ARTICLES
https://doi.org/10.1038/s41566-021-00923-7

nature photonics

Electrically tunable nonlinear polaritonic metasurface

Jaeyeon Yu[1], Seongjin Park[1], Inyong Hwang[1], Daeik Kim[1], Frederic Demmerle[2], Gerhard Boehm[2], Markus-Christian Amann[2], Mikhail A. Belkin[2] and Jongwon Lee[1]✉

Nonlinear polaritonic metasurfaces created by the coupling of intersubband nonlinearities in semiconductor heterostructures with optical modes in nanoresonators have recently demonstrated efficient frequency mixings at very low pumping intensities of the order of a few tens of kilowatts per square centimetre. In these subwavelength structures, the efficiency, spectral bandwidth and local nonlinear phase of wave mixing do not depend on phase matching but only on the nonlinear response of the constituent meta-atoms. We exploit this property to demonstrate an electrically tunable nonlinear metasurface that combines a plasmonic nanocavity and a quantum-engineered semiconductor heterostructure, in which the magnitude and phase of the local nonlinear responses are controlled by a bias voltage through the quantum-confined Stark effect. We demonstrate spectral tuning, dynamic intensity modulation and dynamic beam manipulation for second-harmonic generation. Our work suggests a route for electrically reconfigurable flat nonlinear optical elements with versatile functionalities.

Optical metasurfaces constructed as two-dimensional assemblies of engineered subwavelength structures—capable of controlling local scattering amplitude, phase, and polarization states—have opened an entirely new way of manipulating light and gave rise to the concept of flat optics[1]. In the past decade, research on electrically reconfigurable metasurfaces that can extend the functionalities of passive flat-optics components has been of particular interest, since they can provide a platform enabling the dynamic manipulation of light for a wide range of applications[2–4]. Similar to their linear counterparts, nonlinear metasurfaces that generate nonlinear optical responses in two-dimensional assemblies of engineered subwavelength resonators open new avenues for flat nonlinear optics that can have substantial advantages over bulk nonlinear crystals such as relaxed phase-matching constraints and an ability to engineer the phase and amplitude of nonlinear responses at a deep-subwavelength scale[5–8]. Nonlinear metasurfaces have shown new possibilities for innovative applications, including nonlinear holography[9–13], optical encryptions[14–17], nonlinear optical switching and modulation[18,19], and new frequency generations based on nonlinear frequency mixing[5,6]. To realize such applications for flat nonlinear optics, various nonlinear platforms using plasmonic[20–22] or dielectric structures[23–26] for efficient second-harmonic generation (SHG) and third-harmonic generation in subwavelength films have been studied. However, these structures are mostly composed of passive resonators using materials with intrinsically low nonlinear response and no electrical tuning. A few studies employing plasmonic or dielectric metasurfaces have demonstrated the electrical modulation of the amplitude of nonlinear response based on electric-field-induced SHG or optical rectification[27–30], but the nonlinear response in these structures was very weak and could only be observed using high-intensity femtosecond laser pulses.

Recently, nonlinear intersubband polaritonic metasurfaces comprising plasmonic nanocavities filled with a multiple quantum well (MQW) layer with giant nonlinear optical responses were studied[7,31–34]. Owing to the resonant nonlinearities associated with intersubband transitions (ISTs) between the quantized electron subbands in an n-doped conduction band of a semiconductor heterostructure, the MQW structures can produce giant second-order ($\chi^{(2)}_{zzz}$) and third-order ($\chi^{(3)}_{zzzz}$) nonlinear responses for the optical fields polarized along the surface normal direction (z direction here)[35,36]. The values of these nonlinearities can be four to five orders of magnitude larger than that in natural nonlinear materials. Nonlinear polaritonic metasurfaces combined with the giant intersubband nonlinear response of the MQW enable efficient frequency conversions in a subwavelength thin film using only moderate pump intensities of approximately few tens of kilowatts per square centimetre. In particular, SHG conversion efficiency of 0.083% was reported in the mid-infrared range using a peak pump intensity of only 10 kW cm^{-2} (ref. [33]). An ability to electrically control the nonlinear response of the meta-atoms constituting the nonlinear intersubband polaritonic metasurfaces will allow one to tune their spectral bandwidth and to modulate the phase and amplitude of the nonlinear response by bias voltage at the individual nanoresonator level, leading to a new class of electrically reconfigurable flat nonlinear optics.

Here we employ the Stark tuning of intersubband nonlinearities[37] to demonstrate, for one of the first times, electrically tunable nonlinear response in intersubband polaritonic metasurfaces. The MQW structure used in this work comprises a coupled three-quantum-well system in which the centres of the first three electron subbands that provide giant second-order nonlinear response $\chi^{(2)}_{zzz}$ are spatially separated so that the broadband spectral tuning of $\chi^{(2)}_{zzz}$ can be induced through the quantum-confined Stark effect. By combining plasmonic nanocavity structures capable of generating SHG in free space and applying bias voltages to the MQW layer, spectral tuning, intensity and phase modulation of SHG were achieved for a pump wavelength of around 10 μm.

The concept underlying the operation of our electrically tunable nonlinear metasurface is illustrated in Fig. 1a. The metasurface was constructed using an array of plasmonic nanocavity meta-atoms, with a 400-nm-thick $In_{0.53}Ga_{0.47}As/Al_{0.48}In_{0.52}As$ MQW layer sandwiched between a top Au plasmonic nanoantenna and an optically

[1]Department of Electrical Engineering, Ulsan National Institute of Science and Technology (UNIST), Ulsan, Republic of Korea. [2]Walter Schottky Institute, Technical University of Munich, Garching, Germany. ✉e-mail: jongwonlee@unist.ac.kr

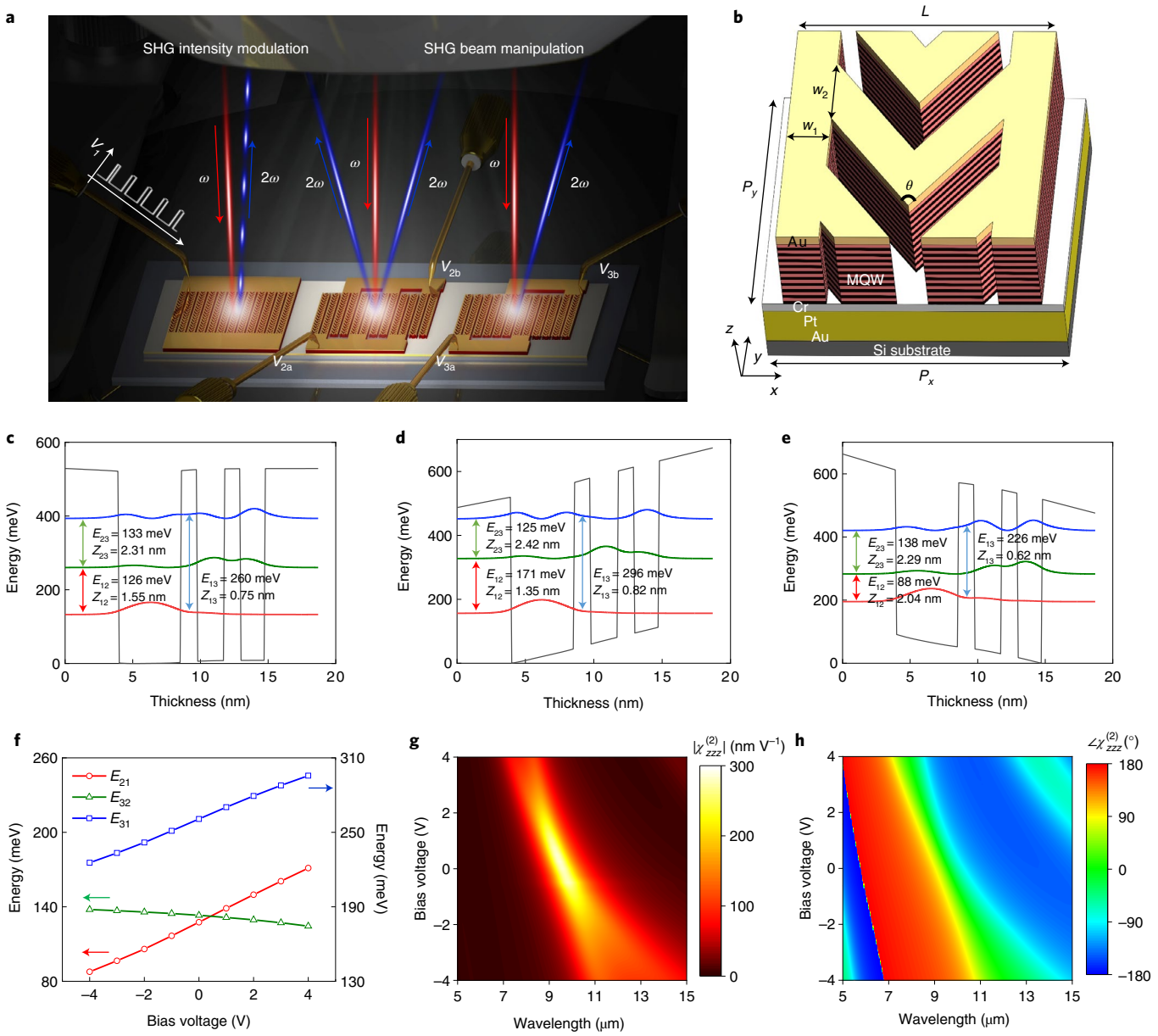

Fig. 1 | Electrically tunable nonlinear polaritonic metasurface. a, Schematic of an electrically tunable nonlinear polaritonic metasurface and its use for SHG intensity modulation (left), SHG beam diffraction (middle) and SHG beam steering (right) as reported in this paper. **b**, Schematic of the meta-atom unit structure. The dimensions are $w_1 = 270$ nm, $w_2 = 380$ nm, $P_x = 1{,}450$ nm, $P_y = 1{,}200$ nm, $L = 1{,}200$ nm and $\theta = 57.6°$. **c**–**e**, Conduction-band diagram of the $In_{0.53}Ga_{0.47}As/Al_{0.48}In_{0.52}As$ coupled three-quantum-well unit structure under 0 V (**c**), +4 V (**d**) and −4 V (**e**). The values of E_{ij} and z_{ij} indicate the computed energy separation and transition dipole element, respectively, between electron states i and j. **f**, Calculated IST energies under different bias voltages. **g**,**h**, Calculated magnitude (**g**) and phase (**h**) of the second-order nonlinear susceptibility of the MQW structure $\chi^{(2)}_{zzz}(V)$ for SHG as functions of the input pump wavelengths (x axis) and applied bias voltages (y axis).

thick bottom Au ground plane (Fig. 1b). The two metallic layers within the plasmonic nanocavity were used as contact layers for applying bias voltages to the MQW layer. In this configuration, SHG is produced in reflection, and the nonlinear optical response can be tuned by the applied bias voltage to the metasurface. Due to the Stark tuning of the resonant intersubband nonlinearity in the MQW structure, both amplitude and phase of the nonlinear response of constituent meta-atoms can also be electrically tuned, enabling dynamic nonlinear beam manipulation.

Figure 1c–e shows the conduction-band diagram of a single period of the MQW heterostructure used in our sample for applied bias voltages of 0, +4 and −4 V, respectively, over a 400-nm-thick MQW layer. The MQW layer consists of twenty repetitions of the MQW periods shown in Fig. 1c–e. The MQW heterostructure was designed to provide giant nonlinear response and to have the first, second and third electron subband confined predominantly in the left, middle and right quantum wells, respectively. The IST energy, E_{ij}, between electron subbands i and j can then be tuned by the bias voltage applied to the MQW layer through the quantum-confined Stark effect. The dependence of the IST energies between the first three electron states on the bias voltage ranging from −4 to +4 V is shown in Fig. 1f.

The SHG nonlinear response of the MQW structure is produced by the resonant transitions among the three electron subbands;

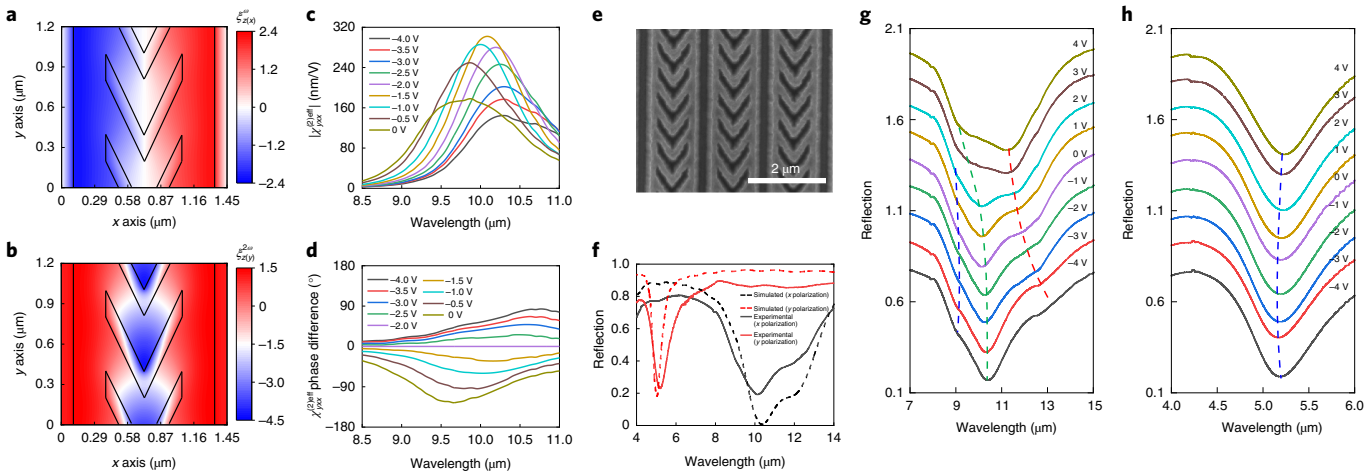

Fig. 2 | Numerical simulations and linear characterization of the metasurface. a,**b**, Top-view cross-section of the normalized E_z field enhancement distribution at the FF with *x*-polarized input *E* field ($\xi^{\omega}_{z(x)} = E^{\omega}_z/E^{\omega}_{x,\mathrm{inc}}$ (**a**)) and at the SH frequency with *y*-polarized input *E* field ($\xi^{2\omega}_{z(y)} = E^{2\omega}_z/E^{2\omega}_{y,\mathrm{inc}}$ (**b**)). The E_z field enhancement was monitored at 100 nm below the top surface of the MQW layer. **c**,**d**, Calculated spectral dependence of the magnitude (**c**) and phase (**d**) of $\chi^{(2)\mathrm{eff}}_{yxx}(V)$ as a function of the pump wavelengths for different bias voltages. The phase of $\chi^{(2)\mathrm{eff}}_{yxx}(V)$ is given in **d** relative to its value at a bias voltage of −2 V: $\angle\chi^{(2)\mathrm{eff}}_{yxx}(V) - \angle\chi^{(2)\mathrm{eff}}_{yxx}(-2V)$. **e**, SEM image of the fabricated metasurface. **f**, Simulated (dashed curve) and measured (solid curve) linear reflection spectra of the metasurface at 0 V for *x*-polarized (black) and *y*-polarized (red) light at normal incidence. **g**,**h**, Measured reflection spectra of the metasurface under *x*-polarized (**g**) and *y*-polarized (**h**) incident light and a d.c. bias voltage ranging from −4 to +4 V with 1 V increments. For a clearer display of the data, the reflection spectra at different bias voltages are vertically offset from each other by 0.15.

therefore, the tensor element of intersubband nonlinear susceptibility as a function of the bias voltage can be expressed as[35,36]

$$\chi^{(2)}_{zzz}(\omega \to 2\omega,\ V) \approx \frac{e^3 N_e}{\varepsilon_0} \frac{Z_{12}(V)Z_{23}(V)Z_{31}(V)}{\left(\hbar\omega_{13}(V) - 2\hbar\omega - \mathrm{i}\hbar\gamma_{13}\right)\left(\hbar\omega_{12}(V) - \hbar\omega - \mathrm{i}\hbar\gamma_{12}\right)}, \quad (1)$$

where ω is the pump frequency; e is the electron charge; N_e is the averaged electron density; ħ is the reduced Planck constant; $\hbar\omega_{ij}(V) = E_{ij}$ and $eZ_{ij}(V)$ denote the IST energy and dipole moment, respectively, as a function of bias voltage V; and $\hbar\gamma_{ij}$ is the linewidth for the IST between electron subbands i and j. Figure 1g shows the calculated magnitude of $\chi^{(2)}_{zzz}$ as functions of both bias voltage and pump wavelength. At 0 V, the $\chi^{(2)}_{zzz}$ peak value of 283 nm V^{-1} occurs at a wavelength of 9.6 μm. As the positive bias is applied to the MQW layer, the wavelength position of peak $\chi^{(2)}_{zzz}$ shifts to a shorter wavelength owing to the increase in E_{12} and E_{13} (Fig. 1f) and the opposite trend is observed for the negative bias. The results show that the maximum of $\chi^{(2)}_{zzz}$ can be tuned in the 8–11 μm wavelength range by applying bias voltages. Figure 1h shows the calculated phase of $\chi^{(2)}_{zzz}$ as functions of both bias voltage and pump wavelength. The phase of $\chi^{(2)}_{zzz}$ can be largely tuned by the bias voltage near the 10 μm wavelength. The dependence of the amplitude and phase of $\chi^{(2)}_{zzz}$ on the bias voltage allows one to electrically control both magnitude and phase of the nonlinear response of a meta-atom in the intersubband polaritonic nonlinear metasurfaces.

The designed MQW structure was grown by molecular-beam epitaxy on a semi-insulating InP substrate; its intersubband absorption measurement result is illustrated in Supplementary Fig. 1 (Methods and Supplementary Information). The measured E_{12} and E_{13} values were 13 meV and 19 meV smaller than the design values, respectively (Fig. 1c) and the measured E_{23} value was well matched with the design value.

To achieve efficient SHG based on the electrically tunable giant nonlinear response of the MQW, we designed a meta-atom structure using a complementary V-shaped nanoantenna with a gap in the *x* direction between the neighbouring unit cells (Fig. 1b). The antenna comprises a structure in which two load lines are connected to a V-shaped antenna that can induce double dipole resonance for two cross-polarized light. In such a structure, plasmonic resonances at the fundamental frequency (FF) and second-harmonic (SH) frequency are easily tuned by adjusting the antenna length (L) and bending angle (θ). The MQW region without the top Au nanoantenna was etched. The etching provides an additional confinement of the optical fields in the MQW material and increases the vertical-field enhancement in the nanoresonators[32]. At the same time, our antenna configuration allows for the easy electrical biasing of individual rows of antennas. The meta-atom structure was designed to induce the enhanced local E_z field in the MQW layer at the FF ω (Fig. 2a) and SH frequency 2ω (Fig. 2b) for *x*- and *y*-polarized input beams, respectively. The effective nonlinear susceptibility of the meta-atom in the metasurface can be expressed as[7]

$$\chi^{(2)\mathrm{eff}}_{ijk}(V) = \chi^{(2)}_{zzz}(V) \left[\int_{v_{\mathrm{MQW}}} \xi^{2\omega}_{z(i)}(x,y,z,V)\xi^{\omega}_{z(j)}(x,y,z,V)\xi^{\omega}_{z(k)}(x,y,z,V)\mathrm{d}v\right]/v_{\mathrm{unit}}, \quad (2)$$

where V is the applied voltage to the MQW structure, $\xi^{\omega \text{ or } 2\omega}_{z(i)} = E^{\omega \text{ or } 2\omega}_{z,\mathrm{MQW}}/E^{\omega \text{ or } 2\omega}_{i,\mathrm{inc}}$ is the enhancement factor of the E_z field in the MQW region ($E^{\omega}_{z,\mathrm{MQW}}$ or $E^{2\omega}_{z,\mathrm{MQW}}$) normalized to the incident *E* field polarized in the *i* direction ($E^{\omega}_{i,\mathrm{inc}}$ or $E^{2\omega}_{i,\mathrm{inc}}$) at FF ω or SH frequency 2ω, v_{unit} and v_{MQW} are the MQW volume in the metasurface unit cell before and after etching, respectively. The volume integral in the square brackets in equation (2) is referred to as the overlap integral. The highest effective nonlinear susceptibility of our metasurface is produced for the *yxx* polarization combination, where the first letter refers to SH polarization and the last two letters refer to FF input pump polarization. Figure 2a,b shows the field enhancement factors $\xi^{\omega}_{z(x)}$ and $\xi^{2\omega}_{z(y)}$, respectively, which are used to compute $\chi^{(2)\mathrm{eff}}_{yxx}$ in equation (2). Figure 2c,d shows the calculated magnitude spectra of $\chi^{(2)\mathrm{eff}}_{yxx}$ and the relative phase difference spectra of $\chi^{(2)\mathrm{eff}}_{yxx}$ defined as the phase difference with respect to the phase response at −2 V, respectively, for the bias voltage ranging from −4.0 to 0 V with a 0.5 V step. Thus, both magnitude and phase of $\chi^{(2)\mathrm{eff}}_{yxx}$ of the meta-atom structure can be strongly modulated near

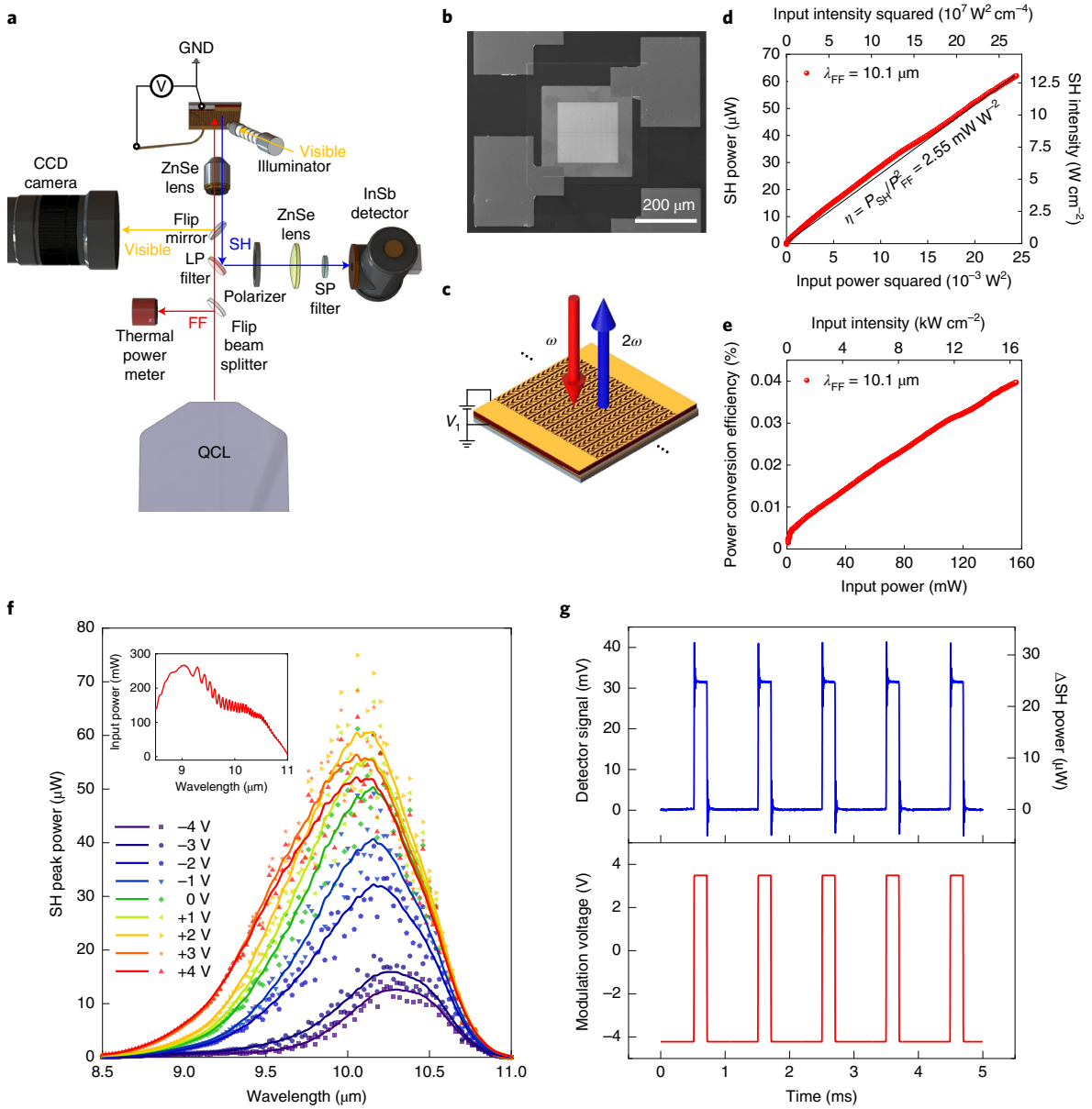

Fig. 3 | Nonlinear characterization of the electrically tunable metasurface. a, Optical setup for the measurement of the SH signal from the metasurface under a bias voltage. The linearly polarized input beam at FF (red arrow) from a QCL was passed via an interference long-wavelength pass (LP) filter operated as a dichroic beam splitter to transmit the FF and reflect the SH frequency and was focused onto the metasurface with a ZnSe aspheric lens. The SH signal (blue arrow) generated from the metasurface was collected by the same lens, reflected by the LP filter and directed to the InSb detector via a linear polarizer, a ZnSe lens and a short-wavelength pass (SP) filter. The flip mirror and flip beam splitter were used only for sample alignment and power monitoring, respectively. **b**, SEM image of the metasurface used for basic nonlinear characterization. **c**, Schematic of the metasurface measurement configuration. **d**, Measured SH peak power (left *y* axis) and intensity (right *y* axis) as a function of the squared input pump power (bottom *x* axis) or squared input intensity (top *x* axis) at a pump wavelength of 10.1 μm. **e**, Measured SH power conversion efficiency as a function of the input pump power (bottom *x* axis) or input intensity (top *x* axis) at a pump wavelength of 10.1 μm. **f**, Measured SH power spectra (dot, measured data; line, moving average) as a function of the wavelength of the input pump for different d.c. bias voltages from −4 to +4 V with a 1 V step. Inset: FF input power spectra used for the measurement. **g**, Dynamic SHG signal modulation by the applied voltage at a pump wavelength of 9.48 μm. Top and bottom panels are the time dependence of the InSb detector signal and the corresponding SHG power change (ΔSH power; top) for the square-modulation bias voltage between −4 and +4 V with a 10% duty cycle at a 1 kHz frequency (bottom).

10 μm wavelength by voltage tuning the intersubband nonlinearity, $\chi^{(2)}_{zzz}(V)$ (Fig. 1g,h). It should be noted that the phase response of $\chi^{(2)\text{eff}}_{yxx}$ is determined by the interaction of $\chi^{(2)}_{zzz}$ with the induced E_z fields in the MQW layer. The phase tuning of $\chi^{(2)\text{eff}}_{yxx}$ due to the bias voltage has a maximum value of 163° near the intersubband resonant wavelength of 10 μm, which is smaller than the maximum phase tuning of $\chi^{(2)}_{zzz}$ due to the influence of the phase response of the induced E_z fields.

For experimental demonstration, we fabricated metasurfaces with a 200 μm × 200 μm two-dimensional array of unit cells (Methods and Supplementary Fig. 2). The design of the unit cell was optimized to provide strong SHG response at a wavelength of 10 μm. Scanning electron microscopy (SEM) image of the fabricated

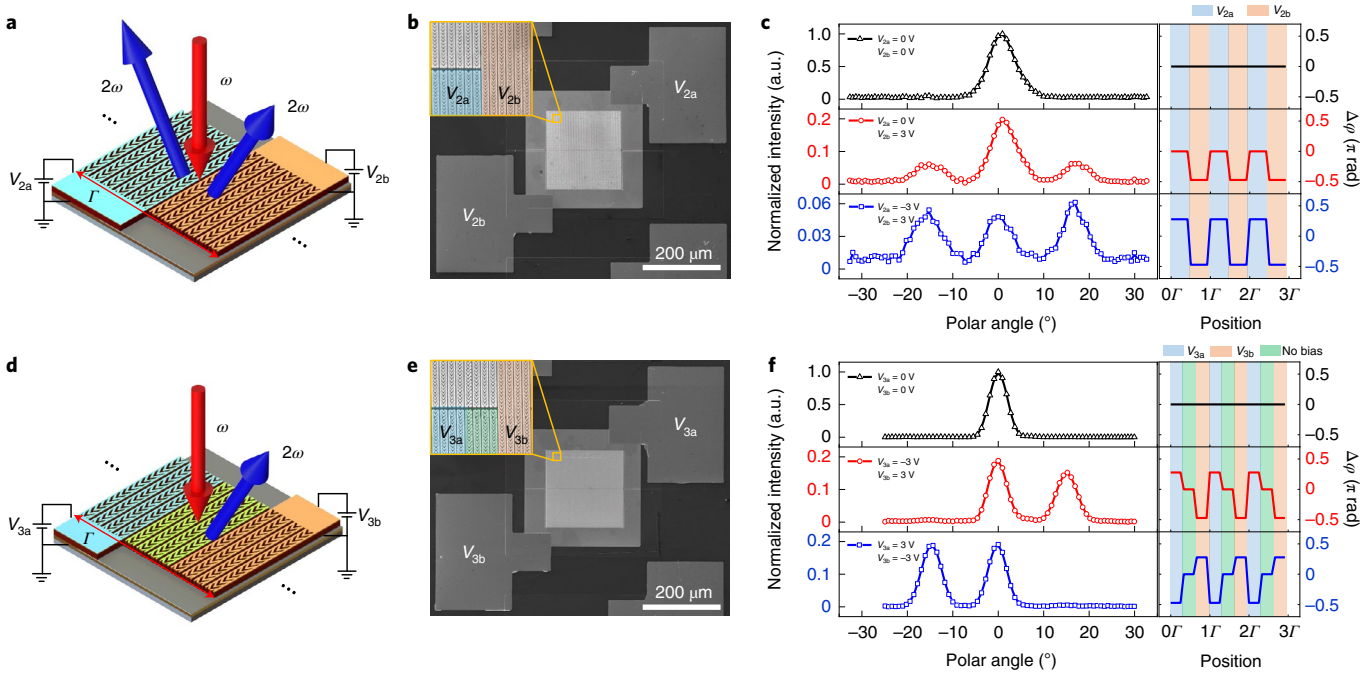

Fig. 4 | Dynamic nonlinear beam manipulations. a, Schematic of the electrically tunable nonlinear phase-grating metasurface constructed by repeating the grating unit period Γ 11 times. The pump beam was incident normally to the metasurface. **b**, SEM image of the processed tunable nonlinear phase-grating metasurface. Inset: zoomed-in view of the one-period edge of the contact formation where two different bias voltages, namely, V_{2a} and V_{2b}, are applied to the blue and red repeating sections of the metasurface, respectively. **c**, Experimental measurements of the far-field profiles of the SHG signal normalized to the peak SHG signal at $V_{2a} = V_{2b} = 0$ for three different bias conditions (left) and the corresponding phase profiles of the nonlinear response (right) from the calculation results shown in Fig. 2d. **d**, Schematic of the electrically tunable nonlinear phase-gradient metasurface constructed by repeating the super-cell period Γ 11 times. **e**, SEM image of the processed tunable nonlinear-gradient metasurface. Inset: zoomed-in view of the one-period edge of the contact formation where two different bias voltages, namely, V_{2a} and V_{2b}, are applied to the blue and red repeating sections, respectively, and no voltage is applied to the green repeating section in the middle. **f**, Experimental measurements of the far-field profiles of the SHG signal normalized to the peak SHG signal at $V_{3a} = V_{3b} = 0$ for three different bias conditions (left) and the corresponding phase profiles of the nonlinear response (right) from the calculation results shown in Fig. 2d.

metasurface is shown in Fig. 2e. Figure 2f shows the simulated and measured linear reflection spectra of the metasurface for *x*- and *y*-polarized light at normal incidence. For the *x*-polarized light, polaritonic reflection peak splitting[38] was observed near a wavelength of 10.5 μm, which is caused by a strong coupling of the cavity mode and IST between the ground and first excited states in the MQW heterostructure, which is a necessary condition for efficient SHG. For the *y*-polarized illumination, strong absorption was observed due to a resonance near a wavelength of 5 μm, which is a necessary condition for efficient out-coupling of the SH nonlinear polarization generated in the MQW region to free space[39]. To confirm the electrical tuning of ISTs and the corresponding polaritonic spectral tuning, linear reflection spectra were measured by applying d.c. bias voltages ranging from −4 to +4 V with a 1 V step (Fig. 2g,h) for the *x*- and *y*-polarized illumination, respectively. In Fig. 2g, the polaritonic peak splitting (green and red dashed curves) due to the strong coupling of the cavity mode and the IST between the ground and the first excited electron states was tuned by changing the bias voltage from +4 to −4 V, as expected from the computed dependence of E_{12} on the bias voltage (Fig. 1f). As the negative bias voltage was increased, additional peak splitting (blue and green dashed curves) resulting from the relatively weak coupling with the IST between states 2 and 3 was also observed. In Fig. 2h, *y*-polarized linear reflection spectra near the SH wavelength exhibit no major changes regardless of the applied bias voltage. The observed linear metasurface spectra at different bias voltages are in general agreement with the simulation results, as discussed in the Supplementary Information and Supplementary Fig. 3 (Supplementary Fig. 4 provides the current–voltage characteristics of the device).

For nonlinear optical characterization, a wavelength-tunable quantum cascade laser (QCL) and a calibrated InSb photodetector were used. The optical setup used for the SHG signal measurement is shown in Fig. 3a (Methods) and the SEM image of the metasurface used for the basic nonlinear optical characterization is shown in Fig. 3b. A schematic of the device configuration is illustrated in Fig. 3c. We first measured the SH peak power (P_{SH}) and intensity (I_{SH}) output from the metasurface as a function of the squared input peak power and squared input peak intensity at the optimal operating pump wavelength of 10.1 μm at 0 V, as shown in Fig. 3d. The corresponding SHG power conversion efficiency P_{SH}/P_{FF} as a function of FF input pump power (P_{FF}) and intensity (I_{FF}) is shown in Fig. 3e. The metasurface exhibits an SHG power conversion efficiency of 0.04% with an input pump peak power of 156 mW and a peak intensity of 16.4 kW cm^{-2}, resulting in an SHG peak power of 62 μW. In addition, we measured the SH signal using a CO_2 laser at 10.6 μm wavelength and achieved an SHG power conversion efficiency of 0.24% and a corresponding SH peak power of 10.8 mW for a pump power of 4.5 W (Supplementary Fig. 5), which is the one of the highest ever reported values based on nonlinear metasurfaces for SHG[40]. The nonlinear conversion factor $\eta = P_{SH}/(P_{FF})^2$ for the metasurface for pump intensity up to 16.4 kW cm^{-2} was 2.55 mW W^{-2}. SHG intensity saturation was not severe due to the relatively low and evenly distributed field enhancements at FF (Fig. 2a) and low pump intensity compared with the previously reported studies[31,32].

Next, we measured the SHG output power spectra of the metasurface by applying d.c. bias voltages varying from +4 V to −4 V with a 1 V step across the entire array (Fig. 3f). As the bias voltage was changed from −4 to +4 V, the SHG spectral peak was tuned from 10.3 μm of the pump wavelength to 10.05 μm, which is consistent with the expected changes in the effective nonlinear response of the meta-atom (Fig. 2c). The simulation results shown in Fig. 2c indicate somewhat larger SHG signal modulation and broader SHG spectral-peak tuning than the measurement. This is because the simulation assumed a uniform electric field over the entire depth of the 400-nm-thick MQW layer. However, due to the formation of the Schottky contacts in the processed metasurface, major band bending occurs near the top or bottom MQW surface for negative or positive bias voltages, respectively, as discussed in the Supplementary Information and shown in Supplementary Fig. 6.

Owing to the strong SH peak power modulation and SHG spectral-peak tuning, it is possible to achieve dynamic modulation of the SHG signal by bias voltage at a fixed pump wavelength. Figure 3g shows the experimental differential photodetector signal and the corresponding SHG output power difference ($\Delta P_{SH} = P_{SH}(4V) - P_{SH}(-4V)$) at a pump wavelength of 9.48 μm, which is the wavelength that can achieve the maximum depth of SHG signal modulation. Square voltage pulses in the range from −4 to +4 V were used for SHG intensity modulation. The SHG signal modulation depth ($\Delta P_{SH}/P_{SH}(-4V)$) of 2,908% was achieved, which is, to the best of our knowledge, a record-high value reported to date[27–29,41]. The resistance–capacitance (*RC*) time constant calculated by considering the device dimensions in the modulated voltage range was 1.67 ns, corresponding to a cutoff SHG modulation frequency of 95 MHz (Supplementary Information).

According to Fig. 2d, the local nonlinear phase of the meta-atom can also be tuned by applying a bias voltage and this property allows one to build nonlinear metasurfaces capable of dynamic nonlinear beam wavefront manipulation. For the experimental demonstration of this effect, we first performed an experiment using an electrically tunable nonlinear phase-grating metasurface (Fig. 4a), in which twelve rows of meta-atoms were used as a phase-grating unit period Γ in the lateral direction ($\Gamma = 12P_x = 17.4\,\mu m$). The metasurface was constructed by repeating the phase-grating period Γ in the lateral direction 11 times. Two different voltages (V_{2a} and V_{2b}) were applied to the two repeating subsections in the grating unit Γ; each of these subsections contained six meta-atoms. This resulted in a rectangular SH phase grating with a 50% duty cycle. The SEM image of the tunable phase-grating metasurface is shown in Fig. 4b. Figure 4c shows the experimental data for three different bias conditions at normal incidence of the pump beam with a wavelength of 10 μm. When $V_{2a} = V_{2b} = 0$ V, only the 0th-order diffraction (specular reflection) was observed for the SHG signal. As the bias conditions were changed to ($V_{2a} = 0$ V and $V_{2b} = +3$ V) and ($V_{2a} = -3$ V and $V_{2b} = +3$ V), the SHG signal in the ±1st-order diffraction at the diffraction angle of ±16.7° ($\theta = \pm\sin^{-1}(\lambda_{SH}/\Gamma)$) appeared. The diffraction sidebands increased in magnitude at a higher difference between V_{2a} and V_{2b} due to the increased phase difference of the SHG signal from the grating subsections. In the case of the square phase grating, the 0th-order diffraction is totally eliminated at a phase difference of π (ref. [42]); however, experimentally, the total elimination of the 0th-order diffraction was not observed. From the relative magnitudes of the 0th- and ±1st-order diffraction peaks and simulation results shown in Supplementary Fig. 7, we estimate that the two grating subsections had an SHG phase difference of about 135° at $V_{2a} = -3$ V and $V_{2b} = +3$ V. Additional experimental data for the other bias conditions are given in Supplementary Fig. 8.

We next performed an experiment using an electrically tunable nonlinear phase-gradient metasurface (Fig. 4d), in which same size of a super-cell period Γ with three different phase sections was used and two different voltages (V_{3a} and V_{3b}) were applied to the left and right subsections, which consist of four rows of meta-atoms, and no voltage was applied to the middle section. The SEM images of the tunable nonlinear phase-gradient metasurfaces is shown in Fig. 4e. Figure 4f shows the experimentally measured far-field profile of the SHG output for three different bias conditions for the 10 μm wavelength pump beam at normal incidence. When $V_{3a} = V_{3b} = 0$ V, the SHG beam was generated and reflected in the surface normal direction; for the positive phase gradient ($V_{3a} = +3$ V, $V_{3b} = -3$ V) and negative phase gradient ($V_{3a} = -3$ V, $V_{3b} = +3$ V), beam steering of the SHG signal was achieved following the generalized Snell's law[1] at angles of either −16.7° (for $V_{3a} = +3$ V, $V_{3b} = -3$ V) or +16.7° (for $V_{3a} = -3$ V, $V_{3b} = +3$ V) (Methods). Experimentally the measured SHG far-field profiles for other bias conditions are shown in Supplementary Fig. 9.

In summary, we reported nonlinear optical metasurfaces in which the amplitude and phase of the nonlinear optical response of an individual meta-atom are controlled by bias voltage via Stark tuning of intersubband nonlinearity. We experimentally demonstrate intensity modulation, beam steering and spectral tuning of the SHG response by the applied bias voltage. These advanced functionalities do not come at the expense of SHG conversion efficiency as our metasurfaces also provide record-high nonlinear optical power conversion efficiency of over 0.2%. Our approach can be extended to other nonlinear optical processes, such as sum- and difference-frequency generation and third-harmonic generation, and the spectral range of the metasurfaces presented here can be extended to near-infrared wavelengths by using materials with larger condition band offsets[43,44]. The electrically tunable nonlinear metasurface may dramatically expand the utility of flat nonlinear optics and create new pathways for innovative applications such as electrically tunable nonlinear light sources, dynamic nonlinear holography, nonlinear information processing and quantum optics.

Online content

Any methods, additional references, Nature Research reporting summaries, source data, extended data, supplementary information, acknowledgements, peer review information; details of author contributions and competing interests; and statements of data and code availability are available at https://doi.org/10.1038/s41566-021-00923-7.

Received: 12 August 2020; Accepted: 25 October 2021;
Published online: 23 December 2021

References

1. Yu, N. F. & Capasso, F. Flat optics with designer metasurfaces. *Nat. Mater.* **13**, 139–150 (2014).
2. Shaltout, A. M., Shalaev, V. M. & Brongersma, M. L. Spatiotemporal light control with active metasurfaces. *Science* **364**, eaat3100 (2019).
3. He, Q., Sun, S. & Zhou, L. Tunable/reconfigurable metasurfaces: physics and applications. *Research* **2019**, 1849272 (2019).
4. Shirmanesh, G. K., Sokhoyan, R., Wu, P. C. & Atwater, H. A. Electro-optically tunable multifunctional metasurfaces. *ACS Nano* **14**, 6912–6920 (2020).
5. Li, G., Zhang, S. & Zentgraf, T. Nonlinear photonic metasurfaces. *Nat. Rev. Mater.* **2**, 17010 (2017).
6. Krasnok, A., Tymchenko, M. & Alu, A. Nonlinear metasurfaces: a paradigm shift in nonlinear optics. *Mater. Today* **21**, 8–21 (2018).
7. Lee, J. et al. Giant nonlinear response from plasmonic metasurfaces coupled to intersubband transitions. *Nature* **511**, 65–69 (2014).
8. Nookala, N. et al. Ultrathin gradient nonlinear metasurface with a giant nonlinear response. *Optica* **3**, 283–288 (2016).
9. Almeida, E., Bitton, O. & Prior, Y. Nonlinear metamaterials for holography. *Nat. Commun.* **7**, 12533 (2016).
10. Ye, W. M. et al. Spin and wavelength multiplexed nonlinear metasurface holography. *Nat. Commun.* **7**, 11930 (2016).
11. Dasgupta, A., Gao, J. & Yang, X. D. Atomically thin nonlinear transition metal dichalcogenide holograms. *Nano Lett.* **19**, 6511–6516 (2019).
12. Reineke, B. et al. Silicon metasurfaces for third harmonic geometric phase manipulation and multiplexed holography. *Nano Lett.* **19**, 6585–6591 (2019).
13. Schlickriede, C. et al. Nonlinear imaging with all-dielectric metasurfaces. *Nano Lett.* **20**, 4370–4376 (2020).

14. Walter, F., Li, G. X., Meier, C., Zhang, S. & Zentgraf, T. Ultrathin nonlinear metasurface for optical image encoding. *Nano Lett.* **17**, 3171–3175 (2017).
15. Ma, M. L. et al. Optical information multiplexing with nonlinear coding metasurfaces. *Laser Photon. Rev.* **13**, 1900045 (2019).
16. Tang, Y. T. et al. Nonlinear vectorial metasurface for optical encryption. *Phys. Rev. Appl.* **12**, 024028 (2019).
17. Zheng, P. X. et al. Metasurface-based key for computational imaging encryption. *Sci. Adv.* **7**, eabg0363 (2021).
18. Lu, C. C. et al. An actively ultrafast tunable giant slow-light effect in ultrathin nonlinear metasurfaces. *Light Sci. Appl.* **4**, e302 (2015).
19. Shcherbakov, M. R. et al. Ultrafast all-optical switching with magnetic resonances in nonlinear dielectric nanostructures. *Nano Lett.* **15**, 6985–6990 (2015).
20. Klein, M. W., Enkrich, C., Wegener, M. & Linden, S. Second-harmonic generation from magnetic metamaterials. *Science* **313**, 502–504 (2006).
21. Celebrano, M. et al. Mode matching in multiresonant plasmonic nanoantennas for enhanced second harmonic generation. *Nat. Nanotechnol.* **10**, 412–417 (2015).
22. Segal, N., Keren-Zur, S., Hendler, N. & Ellenbogen, T. Controlling light with metamaterial-based nonlinear photonic crystals. *Nat. Photon.* **9**, 180–184 (2015).
23. Yang, Y. M. et al. Nonlinear Fano-resonant dielectric metasurfaces. *Nano Lett.* **15**, 7388–7393 (2015).
24. Grinblat, G., Li, Y., Nielsen, M. P., Oulton, R. F. & Maier, S. A. Enhanced third harmonic generation in single germanium nanodisks excited at the anapole mode. *Nano Lett.* **16**, 4635–4640 (2016).
25. Liu, S. et al. An all-dielectric metasurface as a broadband optical frequency mixer. *Nat. Commun.* **9**, 2507 (2018).
26. Koshelev, K. et al. Subwavelength dielectric resonators for nonlinear nanophotonics. *Science* **367**, 288–292 (2020).
27. Cai, W. S., Vasudev, A. P. & Brongersma, M. L. Electrically controlled nonlinear generation of light with plasmonics. *Science* **333**, 1720–1723 (2011).
28. Ding, W., Zhou, L. C. & Chou, S. Y. Enhancement and electric charge-assisted tuning of nonlinear light generation in bipolar plasmonics. *Nano Lett.* **14**, 2822–2830 (2014).
29. Kang, L. et al. Electrifying photonic metamaterials for tunable nonlinear optics. *Nat. Commun.* **5**, 4680 (2014).
30. Lee, K. T. et al. Electrically biased silicon metasurfaces with magnetic Mie resonance for tunable harmonic generation of light. *ACS Photon.* **6**, 2663–2670 (2019).
31. Gomez-Diaz, J. S., Tymchenko, M., Lee, J., Belkin, M. A. & Alu, A. Nonlinear processes in multi-quantum-well plasmonic metasurfaces: electromagnetic response, saturation effects, limits, and potentials. *Phys. Rev. B* **92**, 125429 (2015).
32. Lee, J. et al. Ultrathin second-harmonic metasurfaces with record-high nonlinear optical response. *Adv. Opt. Mater.* **4**, 664–670 (2016).
33. Nookala, N. et al. Mid-infrared second-harmonic generation in ultra-thin plasmonic metasurfaces without a full-metal backplane. *Appl. Phys. B* **124**, 132 (2018).
34. Yu, J. et al. Third-harmonic generation from plasmonic metasurfaces coupled to intersubband transitions. *Adv. Opt. Mater.* **7**, 1801510 (2019).
35. Capasso, F., Sirtori, C. & Cho, A. Y. Coupled-quantum-well semiconductors with giant electric-field tunable nonlinear-optical properties in the infrared. *IEEE J. Quantum Electron.* **30**, 1313–1326 (1994).
36. Rosencher, E. et al. Quantum engineering of optical nonlinearities. *Science* **271**, 168–173 (1996).
37. Sirtori, C., Capasso, F., Sivco, D. L., Hutchinson, A. L. & Cho, A. Y. Resonant Stark tuning of 2nd-order susceptibility in coupled quantum-wells. *Appl. Phys. Lett.* **60**, 151–153 (1992).
38. Todorov, Y. et al. Ultrastrong light-matter coupling regime with polariton dots. *Phys. Rev. Lett.* **105**, 196402 (2010).
39. Balanis, C. A. *Advanced Engineering Electromagnetics* (Wiley, 1989).
40. Wolf, O. et al. Phased-array sources based on nonlinear metamaterial nanocavities. *Nat. Commun.* **6**, 7667 (2015).
41. Chen, S. M., Li, K. F., Li, G. X., Cheah, K. W. & Zhang, S. Gigantic electric-field-induced second harmonic generation from an organic conjugated polymer enhanced by a band-edge effect. *Light Sci. Appl.* **8**, 17 (2019).
42. Harvey, J. E. & Pfisterer, R. N. Understanding diffraction grating behavior: including conical diffraction and Rayleigh anomalies from transmission gratings. *Opt. Eng.* **58**, 087105 (2019).
43. Wolf, O. et al. Enhanced optical nonlinearities in the near-infrared using III-nitride heterostructures coupled to metamaterials. *Appl. Phys. Lett.* **107**, 151108 (2015).
44. Qian, H. L. et al. Large optical nonlinearity enabled by coupled metallic quantum wells. *Light Sci. Appl.* **8**, 13 (2019).

Methods

MQW design and characterization. The coupled three-quantum-well unit structure with $In_{0.53}Ga_{0.47}As/Al_{0.48}In_{0.52}As$ heterostructures was designed by using a self-consistent Poisson–Schrödinger solver. The IST energies and their dipole moment elements according to the applied bias voltages assuming a uniform electric field were calculated using this solver. The layer sequence of the quantum-well unit structure is **4.0**/4.6/**1.2**/2.0/**1.2**/1.8/**4.0** nm, where the boldface indicates $Al_{0.48}In_{0.52}As$ barriers; n doping of $4\times10^{18}\,cm^{-3}$ was injected into the 4.6 nm quantum well. For sample growth, a 300-nm-thick $In_{0.53}Ga_{0.47}As$ etch-stop layer and a 100-nm-thick InP etch-stop layer were grown on a semi-insulating InP substrate; subsequently, the quantum-well unit structure was repeated 20 times to form an MQW layer with a total thickness of 400 nm. Intersubband absorption measurement was performed using a multipath sample piece polished at an angle of 45° on both sides. Using the intersubband absorption measurement, IST energies ($E_{12}=\hbar\omega_{12}\approx113$ meV, $E_{23}=\hbar\omega_{23}\approx135$ meV, $E_{13}=\hbar\omega_{13}\approx241$ meV and $E_{14}=\hbar\omega_{14}\approx340$ meV), transition linewidths ($2\hbar\gamma_{12}\approx20.8$ meV, $2\hbar\gamma_{23}\approx17.6$ meV, $2\hbar\gamma_{13}\approx28.4$ meV and $2\hbar\gamma_{14}\approx28.2$ meV) and average electron density ($N_e\approx0.98\times10^{18}\,cm^{-3}$) in the MQW were extracted (Supplementary Information). For the calculation of the second-order nonlinear susceptibility of the MQW structure, $\chi^{(2)}_{zzz}(V)$ (Fig. 1g,h), we used equation (1) and the transition dipole moment elements and IST energies from the Poisson–Schrödinger calculation. For the calculation of the effective second-order nonlinear susceptibility of the meta-atom structure, $\chi^{(2)eff}_{yxx}(V)$ (Fig. 2c,d), we used equations (1) and (2) and the transition dipole moment elements from the Poisson–Schrödinger calculation and IST energies and transition linewidths from the intersubband absorption measurement.

Numerical simulation. For the meta-atom simulation, we used a finite-difference time-domain solver (Lumerical). The meta-atom structure shown in Fig. 1b was designed by applying periodic boundary conditions in the x and y directions and the perfect matched layer condition in the z direction. The geometric parameters of the complementary V-shaped antenna were determined by using particle swarm optimization. The modal overlap factor was calculated using a $7\times7\times20\,nm^3$ mesh size and integrated over the MQW volume. The built-in dielectric constant of the Au layer in the finite-difference time-domain software was used for device simulation. The MQW layer was modelled as a homogeneous anisotropic medium with out-of-plane and in-plane dielectric constants $\varepsilon_\perp(\omega)$ and $\varepsilon_\parallel(\omega)$, respectively (Supplementary Information and Supplementary Fig. 1). The measured IST energies were used for optimizing the meta-atom structure for actual device processing, and the IST energies from the Poisson–Schrödinger solver were used for the electrically tunable linear and nonlinear response calculation (Fig. 2c,d and Supplementary Fig. 3). There is a slight discrepancy between the design value and measured value of the IST energies; therefore, the electrically tunable linear and nonlinear response simulations of the metasurface were conducted in the negatively shifted bias voltage range from 0 to −4 V (Fig. 2c,d, and Supplementary Fig. 3). For tunable SHG phase-grating simulation (Supplementary Fig. 7), 36 unit structures (three times the grating unit period Γ) with size comparable to the pump beam diameter were used and the SH electric source mode was generated in the unit cell to calculate the far-field profile.

Device fabrication. To transfer the MQW layer onto the metal ground plane, 20 nm Cr, 50 nm Pt and 150 nm Au were deposited as layers on the MQW-layer-grown InP wafer and Si wafer and then thermo-compression wafer bonding was implemented by placing the metal layers of the two wafers in contact with each other. The InP substrate was removed by mechanical polishing and selective chemical etching; subsequently, the 300-nm-thick $In_{0.53}Ga_{0.47}As$ and 100-nm-thick InP etch-stop layers were removed by selective chemical etching. The patterned Au nanoantenna and MQW layer were formed by electron-beam evaporation of 10 nm Cr and 50 nm Au layer, 400 nm SiO_2 layer deposition by RF sputter, electron-beam lithography and a two-step reactive-ion etching process, followed by SiO_2-layer removal in a buffered oxide etchant. A mesa structure with $400\times400\,\mu m^2$ size was formed to prevent current spreading and a 320-nm-thick Si_xN_y passivation layer was deposited on the sample by plasma-enhanced chemical vapour deposition. After forming a pattern opening, a Cr (20 nm)/Cu (300 nm)/Cr (10 nm)/Au (50 nm) top contact layer was patterned. Finally, the sample was mounted on an aluminium plate (thermal sink) using a silver paste. The device fabrication process is illustrated in Supplementary Fig. 2.

Optical characterization. Linear reflection spectra of the metasurfaces were measured by a Fourier transform infrared spectrometer equipped with an infrared microscope (Bruker, VERTEX 70 and HYPERION 1000). For nonlinear optical characterization, a broadly wavelength-tunable QCL capable of both pulse and continuous-wave mode (Daylight Solutions, Mircat system; tuning range, 909–1,230 cm^{-1}; peak power, 400 mW; repetition rate and duty cycle for pulse mode, 100 kHz and 10%, respectively) and a calibrated InSb photodetector (Electro-Optical System; bandwidth (d.c.), 200 kHz) were used (Fig. 3a). The linearly polarized input pump beam from the QCL passes through the LP filter (pass wavelength, >7 μm) and focuses on the metasurface by the ZnSe aspheric lens (numerical aperture, 0.67; effective focal length, 12.5 mm). The generated SH signal is directed to the detector via the LP filter, linear polarizer, ZnSe lens and SP filter (cutoff wavelength, 6 μm). The diameter of the focal spot at the sample position was $2w=49.2\,\mu m$, as confirmed by the knife-edge measurement. A Gaussian intensity profile was assumed for both FF input pump beam ($I_{FF}(r)=I_{FF}e^{-2r^2/w^2}$, $I_{FF}=\frac{2P_{FF}}{\pi w^2}$) and SH beam ($I_{SH}(r)=I_{SH}e^{-4r^2/w^2}$, $I_{SH}=\frac{4P_{SH}}{\pi w^2}$). The average pump power was measured by a thermal power meter (Thorlabs, S302C). The d.c. bias voltage was applied using a sourcemeter (Keithley, SMU 2450) and a d.c. power supply (HP, E3631A). For dynamic SHG signal modulation, a square voltage pulse was applied using a high-voltage pulse generator (HP, 8114A) and the detector signal was monitored using an oscilloscope (Tektronix, TDS2024C). For the nonlinear beam-steering measurements using tunable phase-grating and phase-gradient metasurfaces, we used the same optical setup, except for the output ZnSe lens. The SH signal beam-steering angles were obtained using the lateral shifts at the InSb detector with a pin-hole aperture having a 400 μm diameter by scanning with the detector at a 0.2 mm step in both positive and negative lateral directions, and the lateral-shift distance was converted to an angle. The lateral shift of the signal was given as $f\tan\theta$, where f is the effective focal length of the ZnSe focusing lens and θ is the angle of the harmonic signal with respect to the normal beam path. For the SHG beam steering analysis, we used the phase expression of $[\omega t-kz+\Delta\varphi]$, and in this case, the negative reflection angle is obtained for the positive phase gradient, and vice versa.

Data availability

All the relevant data that support the findings of this study are available from the corresponding author upon reasonable request.

Code availability

All the relevant computing codes that support the findings of this study are available from the corresponding author upon reasonable request.

Acknowledgements

This work was supported by a Basic Science Research Program and Nano Material Technology Development Program through the National Research Foundation of Korea (NRF) under grant nos. 2019R1A2C4070623, 2020R1A4A3079834 and 2018M3A7B4070029 funded by the Korean Government (MSIT). Technical University of Munich group acknowledges support from the DARPA's Nascent Light-Matter Interactions program. This paper is dedicated to the memory of Prof. Markus-Christian Amann who supervised the growth of the semiconductor heterostructure used in this study. Prof. Amann passed away unexpectedly on November 23, 2018.

Author contributions

J.Y. designed the semiconductor heterostructure, calculated the physical parameters, fabricated the device and performed all the experimental measurements and simulations. F.D., G.B., M.-C.A. and M.A.B. performed the semiconductor heterostructure growth. S.P. assisted with the meta-atom design and simulations. I.H. and D.K. assisted with the device fabrication and measurement. J.L. conceived and developed the concept and directed the research. M.A.B., J.Y. and J.L. wrote the manuscript.

Competing interests

The authors declare no competing interests.

Additional information

Supplementary information The online version contains supplementary material available at https://doi.org/10.1038/s41566-021-00923-7.

Correspondence and requests for materials should be addressed to Jongwon Lee.

Peer review information *Nature Photonics* thanks Yuanmu Yang, Shreyas Shah and Maxim Shcherbakov for their contribution to the peer review of this work.

Reprints and permissions information is available at www.nature.com/reprints.